RECONSTRUCTING DYNAMICS FROM STEADY SPATIAL PATTERNS WITH PARTIAL OBSERVATIONS

Anonymous authors
Paper under double-blind review

ABSTRACT

Self-organized spatial patterns, ubiquitous in biological and chemical systems, are often modeled via reaction-diffusion equations. However, real-world scenarios frequently provide only partial observations—such as a single component's steady-state snapshot—challenging the discovery of underlying dynamics. In this work, we address the inverse problem of identifying reaction-diffusion systems from partial observations. We establish the theoretical feasibility of identifying reaction terms and their corresponding coefficients, and introduce a constructive two-stage approach that combines hidden component inference with reaction coefficient identification. Numerical experiments validate the approach's effectiveness. This work provides a novel framework with theoretical guarantees, advancing the study of pattern dynamics with limited data and offering new perspectives for uncovering unknown reaction-diffusion dynamics in real-world scenarios.

1 INTRODUCTION

Spatial pattern formation is a fundamental phenomenon in both natural and engineered systems, underlying diverse processes such as microbial gene expression, tissue organization, animal pigmentation, and chemical reactions (Elowitz & Leibler, 2000; Green & Sharpe, 2015; Epstein & Pojman, 1998; Turing, 1990; Briscoe & Small, 2015). Reaction-diffusion models provide a mathematical framework for studying these emergent patterns, capturing the interplay of local interactions and diffusion (Kondo & Miura, 2010; Nakamasu et al., 2009). Understanding these mechanisms is crucial for deciphering the functional relationships governing pattern formation (Castets et al., 1990).

Reconstructing reaction-diffusion dynamics from incomplete data, however, remains a significant challenge (Stuart, 2010). Observations in real-world scenarios are often constrained to a single system component and limited to steady-state configurations(Chen et al., 2020; Yue et al., 2020), as transient dynamics are either too brief to capture experimentally (Battaglia et al., 2018) or computationally intractable to resolve (Kutz et al., 2016). This challenge is exacerbated in multi-component systems where unobservable variables introduce structural uncertainty, making the inverse problem of identifying reaction-diffusion parameters inherently ill-posed (Engl et al., 1996; Brunton et al., 2020). The steady-state data alone provide little information about temporal evolution, further complicating inference. Additional background on Turing patterns and reaction-diffusion systems, along with related work discussions, is provided in Appendix A.

To address these challenges, we propose a novel framework for identifying reaction-diffusion systems from partial steady-state observations. Unlike conventional approaches that require full spatiotemporal data, our method reconstructs hidden system components and estimates reaction kinetics and diffusion coefficients solely from steady-state spatial distributions. Our contributions include:

- **Hidden component reconstruction**: A latent-space representation, designed specifically for steady-state behavior, enables the recovery of unobserved species while preserving physical consistency.
- **Physics-informed optimization**: By incorporating priors from the reaction-diffusion system, our method ensures theoretical rigor and mitigates the ill-posedness of the inverse problem.

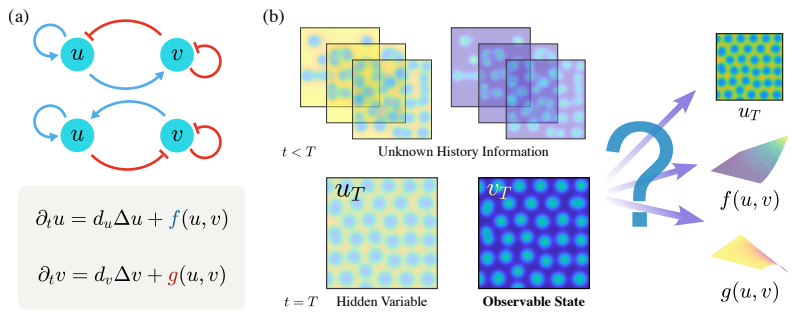

Figure 1: Inverse Problem: System Identification for Reaction-Diffusion Models from Partial Steady-State Observations. (a) Activation-inhibition regulation diagrams illustrating interaction mechanisms and their Governing partial differential equations. (b) The challenge of system identification: only the steady-state spatial distribution of one component (v_T, observable) is available, while historical dynamics and other components (u_T, hidden) remain unknown. Our framework aims to reconstruct underlying dynamics ($f(u,v)$, $g(u,v)$) from limited observations.

- **Joint parameter identification**: Reaction kinetics and diffusion coefficients are inferred simultaneously, capturing both estimation accuracy and physics interpretability.

We validate our method on canonical reaction-diffusion models, including systems exhibiting Turing instabilities and multistability. Numerical experiments demonstrate that our approach effectively reconstructs hidden dynamics and system parameters from highly limited data, offering a principled solution for studying reaction-diffusion processes in biological, chemical, and ecological systems.

2 Problem Formulation

The study of spatial pattern formation originates from Turing's pioneering work on morphogenesis (Turing, 1990). Turing demonstrated that reaction and diffusion processes can destabilize uniform steady states, leading to the emergence of regular spatial patterns, now known as Turing patterns. These processes are typically modeled as coupled partial differential equations

$$\begin{cases} \partial_t u = d_1 \Delta u + f(u,v), \\ \partial_t v = d_2 \Delta v + g(u,v), \end{cases} \quad (x,t) \in \Omega \times (0,\infty), \tag{1}$$

where u and v represent chemical or biological components and f and g shape their reaction process. Under specific parameter regimes, such systems can generate stable spatial patterns. Please see Appendix C.2 for a brief mathematical illustration for the mechanism of pattern formation.

The primary focus of our study is the inverse problem of identifying system parameters from partial, steady-state observations. Specifically, let $u(x,t), v(x,t) \in C^2(\Omega) \times (0,\infty)$ represent the trajectories of (1) under homogeneous Neumann boundary conditions

$$\frac{\partial u}{\partial \nu} = \frac{\partial v}{\partial \nu} = 0, \quad \text{on } \partial\Omega \times (0,\infty). \tag{2}$$

Given access to only a single snapshot $v_T \in C^2(\Omega)$ of the component $v(x,t)$ at time $t = T$, the task is to reconstruct the corresponding u_T and identify the reaction terms $f(u,v)$ and $g(u,v)$.

2.1 Assumptions and Constraints

In general, observing only v_T is insufficient to uniquely determine f, g, and u_T. To address this challenge, we incorporate additional knowledge and assumptions about the system to make the inverse problem solvable.

1. (u_T, v_T) are steady-state Turing Patterns.
2. Diffusive coefficients d_u and d_v are accessible.

3. The space average $\int_\Omega u_T dx/|\Omega|$ is known.
4. f and g belong to a finite-dimensional family $\mathcal{F}$.

By the first assumption, the time derivative of u and v vanish at $t = T$, therefore we have the following correspondences,

$$\begin{cases} d_u \Delta u_T + f(u_T, v_T) = 0, \\ d_v \Delta v_T + g(u_T, v_T) = 0. \end{cases} \tag{3}$$

These equations act as foundations for inferring u_T, and reaction terms f and g. The second and third assumptions are necessary to avoid non-uniqueness of the solution. Refer to Appendix B.1 for constructions of counter-examples without these constraints.

2.2 Finite-Dimensional Basis Representation

Following the fourth assumption from Section 2.1, we define the reaction terms (f, g) as elements of a function family $\mathcal{F}$, spanned by a set of basis functions,

$$\mathcal{F} = \left\{ \sum_{i=1}^{n} a_i \phi_i(u, v) : a_i \in \mathbb{R} \right\}. \tag{4}$$

The basis functions $\{\phi_i(u, v)\}_{i=1}^n$ are selected as candidates to represent specific terms appearing in reaction functions. This formulation is motivated by both practical and theoretical considerations. From a physical perspective, reaction-diffusion systems are governed by physical laws that naturally restrict the functional forms of f and g to the combinations of interpretable components, such as polynomials, exponential functions, or Hill-type terms. From a mathematical standpoint, this finite-dimensional representation ensures the problem's well-posedness (please see details in Appendix B.3); without such constraints, the inverse problem could become highly ill-posed and computationally intractable.

After specifying the set of candidate basis functions $\{\phi_i\}_{i=1}^n$, our task reduces to identifying both the steady-state $u_T \in C^2(\Omega)$ and the coefficients $\{a_i\}_{i=1}^n$ and $\{b_i\}_{i=1}^n$, such that the observed snapshot v_T is consistent with the reaction-diffusion system (1). It has the form

$$\begin{cases} d_u \Delta u_T + \sum_{i=1}^n a_i \phi_i(u_T, v_T) = 0, \\ d_v \Delta v_T + \sum_{i=1}^n b_i \phi_i(u_T, v_T) = 0. \end{cases} \tag{5}$$

3 Methodology

We propose a framework for identifying reaction-diffusion systems by integrating neural network-based state estimation with physics-informed optimization to infer hidden dynamics and estimate reaction terms. Let v_T be the observable state at time T, and u_T the latent state. For simplicity, we denote them as v and u, with $\hat{\cdot}$ representing estimations. Basis functions $\{\phi_i\}_{i=1}^n$ span the function family $\mathcal{F}$.

3.1 Architecture Design

Our framework consists of two modules: **State Estimator** and **Reaction Term Estimators**, designed for hidden state reconstruction and reaction term estimation.

The **State Estimator** is a CNN-based network $u_{\text{NN}} : \mathbb{R}^{N_x \times N_y \times 2} \to \mathbb{R}^{N_x \times N_y}$ mapping $(v, \Delta v)$ to an estimated state

$$\hat{u} = u_{\text{NN}}(v, \Delta v; \theta_u), \tag{6}$$

where θ_u are trainable parameters. Importantly, u_{NN} performs a mapping between functions rather than point-wise values, such that in each forward step, it takes the entire functions v and Δv as inputs and returns the function $\hat{u}$. This approach ensures that the inference process has access to local information, which is necessary since there is no guaranteed one-to-one correspondence between $v(x)$, $\Delta v(x)$, and $u(x)$.

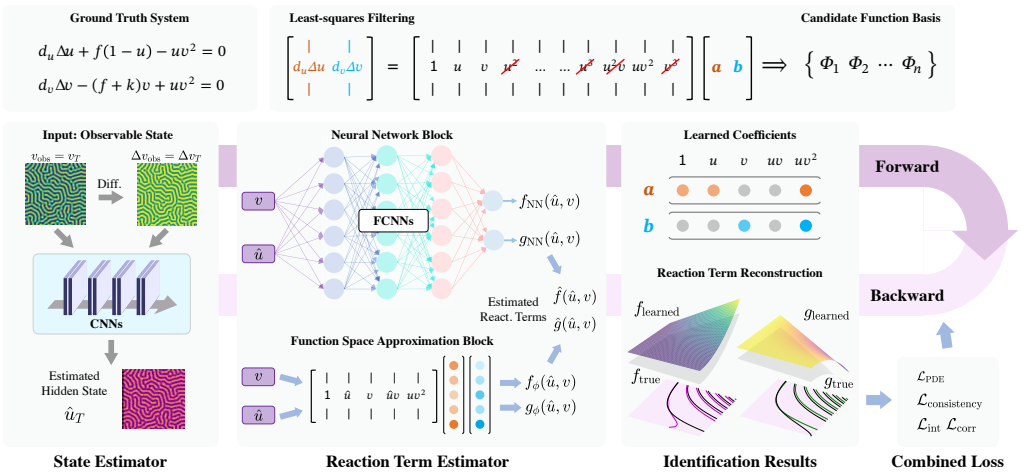

Figure 2: Overview of the proposed identification framework for reaction-diffusion systems.

The **Reaction Term Estimators** approximate the reaction functions f, g and their coefficient $\{a_i\}_{i=1}^n$, $\{b_i\}_{i=1}^n$ respectively using a neural-basis hybrid

$$\begin{aligned} \hat{f}(r,s) &= \alpha f_{\text{NN}}(r,s;\theta_f) + (1-\alpha) f_\phi(r,s;\boldsymbol{a}) \\ \hat{g}(r,s) &= \alpha g_{\text{NN}}(r,s;\theta_g) + (1-\alpha) g_\phi(r,s;\boldsymbol{b}) \end{aligned} \tag{7}$$

where f_{NN} and g_{NN} are fully connected neural networks with learnable parameters θ_f, θ_g. $\alpha \in [0,1]$ is a mixing parameter. f_ϕ and g_ϕ are given as follows,

$$f_\phi = \sum_{i=1}^n a_i \phi_i, \quad g_\phi = \sum_{i=1}^n b_i \phi_i, \tag{8}$$

where $\boldsymbol{a} = \{a_i\}_{i=1}^n$ and $\boldsymbol{b} = \{b_i\}_{i=1}^n$ are learnable coefficients. By using r and s instead of u and v, it is remarked that Reaction Term Estimators take point-wise inputs $(r,s) \in \mathbb{R} \times \mathbb{R}$, which are different from the State Estimator.

In a forward step, the State Estimator first takes the input v and Δv to give $\hat{u}$ as the estimation. Next, $r = \hat{u}(x)$ and $s = v(x)$ for $x \in \Omega$ are forwarded into the Reaction Term Estimators to give the estimation of $\hat{f}(\hat{u}(x), v(x))$ and $g(\hat{u}(x), v(x))$.

3.2 Physics-Informed Optimization

Training is guided by physics-informed loss functions. Let Θ denote all learnable parameters. The steady-state PDE residuals enforce physical constraints,

$$\begin{aligned} \mathcal{L}_u(\Theta) &= \|d_u \Delta \hat{u} + \hat{f}(\hat{u}, v)\|_\Omega^2, \\ \mathcal{L}_v(\Theta) &= \|d_v \Delta v + \hat{g}(\hat{u}, v)\|_\Omega^2. \end{aligned} \tag{9}$$

To enforce the function family assumption, we require the estimators $\hat{f}$ and $\hat{g}$ to closely resemble functions within $\mathcal{F}$ and expect the neural networks f_{NN} and g_{NN} to be consistent with f_ϕ and g_ϕ, which yields the following consistency loss,

$$\mathcal{L}_{\text{cons}}(\Theta) = \|\hat{f}(\hat{u}, v) - f_\phi(\hat{u}, v; \boldsymbol{a})\|_\Omega^2 + \|\hat{g}(\hat{u}, v) - g_\phi(\hat{u}, v; \boldsymbol{b})\|_\Omega^2. \tag{10}$$

Additional losses enforce integral constraints and correlation priors:

$$\begin{aligned} \mathcal{L}_{\text{int}}(\Theta) &= \left(\frac{\int_\Omega \hat{u}(x)dx - \int_\Omega u(x)dx}{\int_\Omega u(x)dx} \right)^2, \\ \mathcal{L}_{\text{corr}}(\Theta) &= \text{Corr}_{x \sim \text{Unif}(\Omega)} \big(\hat{u}(x), v(x)\big). \end{aligned} \tag{11}$$

Here, $\text{Unif}(\Omega)$ stands for the uniform distribution on Ω. By combining all the loss terms, we formulate the overall loss function to guide the training process, $\mathcal{L}_{\text{total}} = \sum_{i=1}^5 \lambda_i \mathcal{L}_i$.

3.3 Two-Stage Training Protocol

Our training protocol implements a physics-informed hierarchical strategy that systematically integrates neural approximation with symbolic regression.

The first stage is a domain-aware coefficient estimation. A moving-window least squares method initializes basis coefficients $\boldsymbol{a}, \boldsymbol{b}$. For each spatial window Ω_w, solve

$$\min_{\{a_{w,i}, b_{w,i}\}} \sum_{(x,y)\in\Omega_w} \left\| \begin{bmatrix} d_u \Delta u + \sum_i a_{w,i}\phi_i(u,v) \\ d_v \Delta v + \sum_i b_{w,i}\phi_i(u,v) \end{bmatrix} \right\|_2^2. \tag{12}$$

Global coefficients are aggregated via spatial averaging

$$a_i = \mathbb{E}_w[a_{w,i}], \quad b_i = \mathbb{E}_w[b_{w,i}]. \tag{13}$$

The second stage involved a joint optimization. All parameters $\Theta = \{\theta_u, \theta_f, \theta_g, \boldsymbol{a}, \boldsymbol{b}, \alpha\}$ are optimized via Adam with adaptive learning rate scheduling

$$\eta_k = \eta_0 \cdot \beta^{\lfloor k/p \rfloor}, \tag{14}$$

where p governs the decay interval. Training terminates when validation loss plateaus for p_{stop} consecutive epochs.

4 Identifiability

We analyze the identifiability of our inverse problem from both theoretical and practical perspectives, with particular attention to the challenges posed by partial observations.

4.1 Identifiability Conditions under Full Observability

We first consider the idealized case where both states (u, v) are fully observable. In this setting, we need to determine whether the basis functions ϕ_i and their coefficients $\boldsymbol{a}, \boldsymbol{b}$ can be uniquely identified from the observed patterns. We rigorously address this through the following

Let $X \in \mathbb{R}^{2N_p \times 2n}$ denote the design matrix constructed from basis evaluations across N_p spatial points (see Appendix B.2). The parameters $\boldsymbol{\beta} = (\boldsymbol{a}, \boldsymbol{b})$ are identifiable if and only if

$$\text{rank}(X) = 2n. \tag{15}$$

This rank condition requires

1) *Non-degenerate Patterns*: Spatial variations in v must excite all basis functions.

2) *Minimum Observation Scale*: $N_p \geq n$, with non-redundant spatial sampling.

3) *Basis Independence*: $\{\phi_i(u, v)\}$ are linearly independent over the observed (u, v). Note that the independence of $\{\phi_i\}$ is distinct from the independence of $\{\phi_i(u, v)\}$.

4.2 Regularized Identifiability under Partial Observation

With only v observed, we address ill-posedness via

1. *Symmetry-Breaking Conditions*: Knowledge of the diffusion coefficients d_u, d_v and the spatial average $\int_\Omega u dx/|\Omega|$ helps eliminate affine symmetry, which avoids non-uniqueness from affine transformation.

2. *Adaptive Coefficient Thresholding*: Insignificant coefficients are pruned via

$$\hat{a}_i = \begin{cases} a_i & \text{if } |a_i| > \tau \cdot \text{MAD}(\boldsymbol{a}) \\ 0 & \text{otherwise,} \end{cases} \tag{16}$$

where MAD is the median absolute deviation and τ is a sensitivity parameter. This suppresses spurious terms while preserving dominant dynamics.

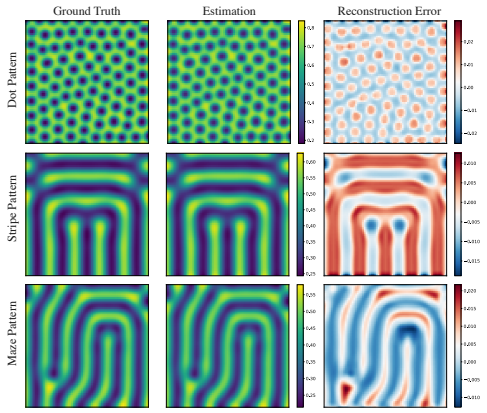

Figure 3: State reconstruction performance for Turing pattern models.

Table 1: Reconstruction errors and computational costs (N_x: spatial resolution).

Pattern	N_x	Error			Time (s)
		u	f	g	
Stripe	75	4.56e-3	1.39e-3	6.21e-4	43.05
	100	5.54e-3	1.79e-3	7.48e-4	72.27
	150	1.27e-2	3.59e-3	1.64e-3	116.20
Dot	75	3.19e-3	5.16e-4	5.19e-4	43.09
	100	1.39e-2	4.04e-4	2.21e-4	55.91
	150	6.36e-3	1.63e-5	8.52e-5	124.56
Maze	75	2.34e-3	1.24e-4	2.00e-4	43.89
	100	2.22e-3	6.38e-4	5.54e-4	56.69
	150	1.28e-2	4.58e-3	6.91e-4	127.78

3. *Local-Global Basis Alignment*: The moving-window least squares in Stage 1 ensures local coefficient diversity, preventing rank collapse from global symmetries. This is critical for patterns with spatially varying dominant terms (e.g., transitioning between activator-inhibitor regimes).

Traditional least squares methods fail under partial observations due to rank deficiency (e.g., unobserved u). Our approach circumvents this limitation by 1) Jointly estimating u and reaction terms, 2) Constraining the solution space via physics-informed losses, 3) Exploiting the inductive bias of convolutional architectures for pattern completion.

5 Experiments

We conduct comprehensive experiments to evaluate our framework's effectiveness in identifying reaction-diffusion systems from partial observations. All experiments were performed on a computational setup with an Intel Xeon Gold 6334 CPU (32 cores, 64 threads) and 64GB RAM. We test the Gray-Scott, Brusselator, and FitzHugh-Nagumo models, generating patterns at spatial resolutions $N_x = 75, 100, 150$. Model and implementation details appear in Appendix C and Appendix D, respectively.

5.1 Pattern Reconstruction and Dynamic Identification

Figure 3 demonstrates accurate hidden state reconstruction (u_T) across pattern types. Table 1 reveals counterintuitive scaling behavior: reconstruction errors *increase* with domain size due to reduced boundary information impact in larger domains. For stripes, the u error rises from 4.56e-3 ($N_x = 75$) to 1.27e-2 ($N_x = 150$). This counterintuitive trend stems from the scale-invariant nature of the Turing mechanism. Under non-periodic boundaries, asymmetries introduce informative features near the edges, while repetitive interior patterns provide less information. As the domain grows, the interior region expands, reducing the relative influence of boundary-induced information on reconstruction.

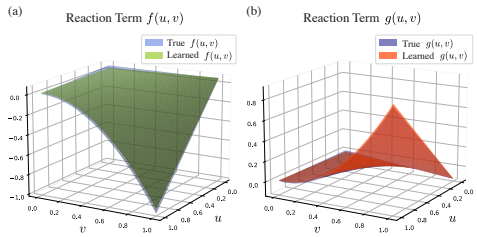

Figure 4: Reaction term identification: Ground truth vs. reconstruction for f(u,v) and g(u,v).

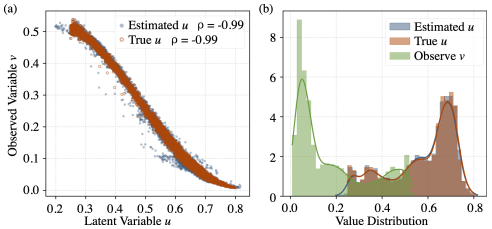

Figure 5: Latent variable correlation: Estimated vs. true u distributions align with $\rho = -0.99$.

Figure 4 demonstrates accurate recovery of reaction terms across nonlinear regimes, with reconstruction fidelity directly tied to u-estimation accuracy (Table 1). The strong u-v anti-correlation in Figure 5 confirms precise latent variable reconstruction, showing >95% distribution overlap between estimated and true u values in critical regions ($u \in [0.3, 0.7]$).

5.2 Noise Robustness Evaluation

We conduct comprehensive experiments to evaluate the robustness of our proposed method under various noise conditions. In our experiments, we consider additive zero-mean Gaussian noise with standard deviation σ times the mean absolute value of the data. The noise level σ is systematically varied from 0.01 to 0.20 to evaluate the impact of noise on performance. Please see the detailed visualization of field reconstructions and sensitivity analysis of reconstruction performance under different noise scenarios in Appendix E.2.

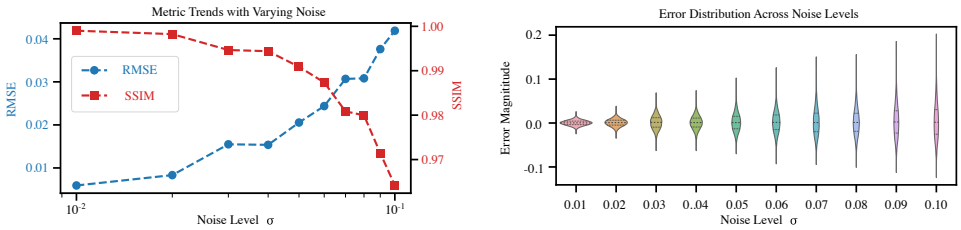

Figure 6: Noise robustness analysis of the dynamic identification framework. Left: quantitative metrics (RMSE and SSIM) with respect to noise level. Right: The distribution of reconstruction errors at different noise levels.

In Figure 6, the proposed method is evaluated under additive Gaussian noise with $\sigma \in [0.01, 0.1]$. Figure 6(a) demonstrates the relationship between noise levels and reconstruction quality metrics. The Root Mean Square Error (RMSE) exhibits a logarithmic relationship with noise intensity ($R^2 = 0.98$), confirming the method's noise robustness, while the Structural Similarity Index Measure (SSIM) maintains values above 0.96 even under significant noise conditions ($\sigma \leq 0.1$), indicating robust preservation of structural information. Figure 6(b) further reveals that 78% of estimation errors remain within ± 0.05 even at $\sigma = 0.1$, indicating strong robustness against outliers. These results collectively validate the method's applicability in real-world noisy environments.

6 Conclusion

We introduce a novel framework for reconstructing reaction-diffusion systems from partial, steady-state observations, addressing a fundamental challenge in dynamical system identification. Our approach infers both hidden variables and reaction terms from a single-component snapshot — an ill-posed problem — by integrating physics-informed learning frameworks with symbolic regression. We establish theoretical identifiability guarantees and demonstrate robust recovery of spatial patterns and governing dynamics across diverse systems. Key innovations include (i) simultaneous learning of latent states and reaction terms via interconnected estimators and (ii) a dual representation of reaction terms for improved accuracy and efficiency. Physical constraints guide learning toward physically consistent solutions, enabling our method to operate under observational sparsity—particularly valuable for biological and chemical systems where transient dynamics are inaccessible.

Limitations include reliance on predefined basis functions, restricting reaction term flexibility, and challenges with high-dimensional hidden states or spatially heterogeneous diffusion. However, the modular design allows future integration of domain-specific constraints. Despite these challenges, our approach opens new avenues for studying self-organization behaviors in experimental systems, enabling researchers to reverse-engineer pattern formation mechanisms. More broadly, it highlights the potential of hybrid machine learning and physics-based methods in tackling foundational inverse problems in complex systems.

REFERENCES

Peter W Battaglia, Jessica B Hamrick, Victor Bapst, Alvaro Sanchez-Gonzalez, Vinicius Zambaldi, Mateusz Malinowski, Andrea Tacchetti, David Raposo, Adam Santoro, Ryan Faulkner, et al. Relational inductive biases, deep learning, and graph networks. *arXiv preprint arXiv:1806.01261*, 2018.

Martin Benning and Martin Burger. Modern regularization methods for inverse problems. *Acta numerica*, 27:1–111, 2018.

James Briscoe and Stephen Small. Morphogen rules: design principles of gradient-mediated embryo patterning. *Development*, 142(23):3996–4009, 2015.

Steven L Brunton, Joshua L Proctor, and J Nathan Kutz. Discovering governing equations from data by sparse identification of nonlinear dynamical systems. *Proceedings of the national academy of sciences*, 113(15):3932–3937, 2016.

Steven L Brunton, Bernd R Noack, and Petros Koumoutsakos. Machine learning for fluid mechanics. *Annual review of fluid mechanics*, 52(1):477–508, 2020.

Vincent Castets, Etiennette Dulos, Jacques Boissonade, and Patrick De Kepper. Experimental evidence of a sustained standing turing-type nonequilibrium chemical pattern. *Physical review letters*, 64(24):2953, 1990.

Kathleen Champion, Bethany Lusch, J Nathan Kutz, and Steven L Brunton. Data-driven discovery of coordinates and governing equations. *Proceedings of the National Academy of Sciences*, 116 (45):22445–22451, 2019.

Ricky TQ Chen, Yulia Rubanova, Jesse Bettencourt, and David K Duvenaud. Neural ordinary differential equations. *Advances in neural information processing systems*, 31, 2018.

Yu Chen, Jin Cheng, Yu Jiang, and Keji Liu. A time delay dynamical model for outbreak of 2019-ncov and the parameter identification. *Journal of Inverse and Ill-posed Problems*, 28(2):243–250, 2020.

Michael B Elowitz and Stanislas Leibler. A synthetic oscillatory network of transcriptional regulators. *Nature*, 403(6767):335–338, 2000.

Heinz Werner Engl, Martin Hanke, and Andreas Neubauer. *Regularization of inverse problems*, volume 375. Springer Science & Business Media, 1996.

Irving R Epstein and John A Pojman. *An introduction to nonlinear chemical dynamics: oscillations, waves, patterns, and chaos*. Oxford university press, 1998.

Ali Feizmohammadi, Yavar Kian, and Gunther Uhlmann. Partial data inverse problems for reaction-diffusion and heat equations. *arXiv preprint arXiv:2406.01387*, 2024.

Richard FitzHugh. Impulses and physiological states in theoretical models of nerve membrane. *Biophysical journal*, 1(6):445–466, 1961.

Laurent Girin, Simon Leglaive, Xiaoyu Bie, Julien Diard, Thomas Hueber, and Xavier Alameda-Pineda. Dynamical variational autoencoders: A comprehensive review. *arXiv preprint arXiv:2008.12595*, 2020.

Peter Gray and Stephen K Scott. Autocatalytic reactions in the isothermal, continuous stirred tank reactor: Oscillations and instabilities in the system a+ 2b→ 3b; b→ c. *Chemical Engineering Science*, 39(6):1087–1097, 1984.

Jeremy Green and James Sharpe. Positional information and reaction-diffusion: two big ideas in developmental biology combine. *Development*, 142(7):1203–1211, 2015.

Daniel Henry. *Geometric theory of semilinear parabolic equations*, volume 840. Springer, 2006.

Victor Isakov. *Inverse problems for partial differential equations*, volume 127. Springer, 2006.

Barbara Kaltenbacher and William Rundell. On the identification of a nonlinear term in a reaction–diffusion equation. *Inverse Problems*, 35(11):115007, 2019.

Barbara Kaltenbacher and William Rundell. The inverse problem of reconstructing reaction–diffusion systems. *Inverse Problems*, 36(6):065011, 2020.

Christopher A Klausmeier. Regular and irregular patterns in semiarid vegetation. *Science*, 284 (5421):1826–1828, 1999.

Shigeru Kondo and Takashi Miura. Reaction-diffusion model as a framework for understanding biological pattern formation. *science*, 329(5999):1616–1620, 2010.

J Nathan Kutz, Steven L Brunton, Bingni W Brunton, and Joshua L Proctor. *Dynamic mode decomposition: data-driven modeling of complex systems*. SIAM, 2016.

Peter Y Lu, Joan Ariño Bernad, and Marin Soljačić. Discovering sparse interpretable dynamics from partial observations. *Communications Physics*, 5(1):206, 2022.

Hans Meinhardt and Alfred Gierer. Applications of a theory of biological pattern formation based on lateral inhibition. *Journal of cell science*, 15(2):321–346, 1974.

Jeff Morgan. Global existence for semilinear parabolic systems. *SIAM journal on mathematical analysis*, 20(5):1128–1144, 1989.

Jeff Morgan and Bao Quoc Tang. Boundedness for reaction–diffusion systems with lyapunov functions and intermediate sum conditions. *Nonlinearity*, 33(7):3105, 2020.

Akiko Nakamasu, Go Takahashi, Akio Kanbe, and Shigeru Kondo. Interactions between zebrafish pigment cells responsible for the generation of turing patterns. *Proceedings of the National Academy of Sciences*, 106(21):8429–8434, 2009.

Jaideep Pathak, Brian Hunt, Michelle Girvan, Zhixin Lu, and Edward Ott. Model-free prediction of large spatiotemporally chaotic systems from data: A reservoir computing approach. *Physical review letters*, 120(2):024102, 2018.

Ilya Prigogine and René Lefever. Symmetry breaking instabilities in dissipative systems. ii. *The Journal of Chemical Physics*, 48(4):1695–1700, 1968.

Maziar Raissi, Paris Perdikaris, and George E Karniadakis. Physics-informed neural networks: A deep learning framework for solving forward and inverse problems involving nonlinear partial differential equations. *Journal of Computational physics*, 378:686–707, 2019.

Chengping Rao, Pu Ren, Qi Wang, Oral Buyukozturk, Hao Sun, and Yang Liu. Encoding physics to learn reaction–diffusion processes. *Nature Machine Intelligence*, 5(7):765–779, 2023.

Max Rietkerk, Robbin Bastiaansen, Swarnendu Banerjee, Johan van de Koppel, Mara Baudena, and Arjen Doelman. Evasion of tipping in complex systems through spatial pattern formation. *Science*, 374(6564):eabj0359, 2021.

Franz Rothe. *Global solutions of reaction-diffusion systems*, volume 1072. Springer, 2006.

Samuel H Rudy, Steven L Brunton, Joshua L Proctor, and J Nathan Kutz. Data-driven discovery of partial differential equations. *Science advances*, 3(4):e1602614, 2017.

Hayden Schaeffer. Learning partial differential equations via data discovery and sparse optimization. *Proceedings of the Royal Society A: Mathematical, Physical and Engineering Sciences*, 473 (2197):20160446, 2017.

Andrew M Stuart. Inverse problems: a bayesian perspective. *Acta numerica*, 19:451–559, 2010.

Alan Mathison Turing. The chemical basis of morphogenesis. *Bulletin of mathematical biology*, 52: 153–197, 1990.

Sifan Wang, Hanwen Wang, and Paris Perdikaris. On the eigenvector bias of fourier feature networks: From regression to solving multi-scale pdes with physics-informed neural networks. *Computer Methods in Applied Mechanics and Engineering*, 384:113938, 2021.

Yan Yue, Chen Yu, Liu Keji, Luo Xinyue, Xu Boxi, Jiang Yu, and Cheng Jin. Modeling and prediction for the trend of outbreak of ncp based on a time-delay dynamic system. *Scientia Sinica Mathematica*, 50(3):385, 2020.

AN Zaikin and AM Zhabotinsky. Concentration wave propagation in two-dimensional liquid-phase self-oscillating system. *Nature*, 225(5232):535–537, 1970.

A Related Work

Recent theoretical breakthroughs have advanced the identifiability of reaction-diffusion systems under partial observations. Kaltenbacher and Rundell (Kaltenbacher & Rundell, 2019; 2020) established uniqueness conditions for reconstructing source terms from sparse temporal data, building on foundational work in elliptic inverse problems (Isakov, 2006). Feizmohammadi et al. (Feizmohammadi et al., 2024) resolved partial-boundary identifiability in semilinear parabolic systems using Carleman estimates. While these works provide rigorous mathematical foundations for addressing ill-posedness in reaction-diffusion inverse problems (Benning & Burger, 2018), computational methods for steady-state systems with hidden variables remain underdeveloped.

Concurrently, machine learning has reshaped dynamical system identification through data-driven and physics-informed approaches. Neural ODEs (Chen et al., 2018) introduced neural parameterizations of vector fields, while sparse regression techniques like SINDy (Brunton et al., 2016) and PDE-FIND (Rudy et al., 2017) enable equation discovery from spatiotemporal data with convergence guarantees under certain functional assumptions (Schaeffer, 2017). Physics-Informed Neural Networks (PINNs) (Raissi et al., 2019) further integrate PDE constraints into training losses, although spectral bias remains a significant challenge (Wang et al., 2021). Hybrid architectures, such as physics-encoded recurrent networks (Rao et al., 2023) and symbolic regression hybrids (Lu et al., 2022; Champion et al., 2019), aim to balance interpretability with flexibility.

Despite these advancements, most approaches rely on extensive spatiotemporal data, making them impractical for cases where only sparse or single steady-state observations are available. Gradient-based inverse methods (Pathak et al., 2018) and latent variable models (Girin et al., 2020) offer potential solutions for limited-data scenarios but lack a unified framework for steady-state system identification. Furthermore, theoretical insights into the ill-posed nature of inverse problems have yet to be fully leveraged in this context. Although these approaches have substantially advanced the field, they predominantly rely on multiple temporal snapshots or rich spatio-temporal data. The fundamental challenge of reconstructing dynamics from partial steady-state observations, along with the mathematical well-posedness of such reconstruction, remains an open problem.

B Derivations and Analysis

B.1 Non-Uniqueness Statement

We provide a simple illustration showing that, given only the steady-state observation v_T and the function family constraints on the reaction terms, multiple combinations of $(u_T, f, g) \in C^2(\Omega) \times \mathcal{F} \times \mathcal{F}$ can satisfy the steady-state reaction-diffusion equation. Suppose $u_T \in C^2(\Omega)$ and $f, g \in \mathcal{F}$ form one such valid combination. Then, we have,

$$\begin{cases} d_u \Delta u_T + f(u_T, v_T) = 0, \\ d_v \Delta v_T + g(u_T, v_T) = 0. \end{cases} \tag{17}$$

By the function family assumption, there exist sets of coefficients $\{a_i\}_{i=1}^n$ and $\{b_i\}_{i=1}^n$ such that $f = \sum_{i=1}^n a_i \phi_i$ and $g = \sum_{i=1}^n b_i \phi_i$. Furthermore, we assume that the basis functions $\{\phi_i\}_{i=1}^n$ on $\mathbb{R}^2$ are separable, which means they can be expressed as $\{\phi_i(u,v)\}_{i=1}^n = \{\varphi_j(u)\psi_k(v)\}_{j,k=1}^{l,m}$. We rewrite (17) as follows,

$$\begin{cases} d_u \Delta u_T + \displaystyle\sum_{k=1}^{m} \sum_{j=1}^{l} a_{jk} \varphi_j(u_T) \psi_k(v_T) = 0, \\ d_v \Delta v_T + \displaystyle\sum_{k=1}^{m} \sum_{j=1}^{l} b_{jk} \varphi_j(u_T) \psi_k(v_T) = 0. \end{cases} \tag{18}$$

Let c be an arbitrary constant. We check whether $\tilde{u}_T = u_T + c$ can be another solution, such that there exist sets of coefficients $\{\tilde{a}_{jk}\}_{j,k=1}^{l,m}$ and $\{\tilde{b}_{jk}\}_{j,k=1}^{l,m}$ satisfying,

$$\begin{cases} d_u \Delta u_T + \sum_{k=1}^{m} \sum_{j=1}^{l} \tilde{a}_{jk} \varphi_j(u_T + c) \psi_k(v_T) = 0, \\ d_v \Delta v_T + \sum_{k=1}^{m} \sum_{j=1}^{l} \tilde{b}_{jk} \varphi_j(u_T + c) \psi_k(v_T) = 0. \end{cases} \tag{19}$$

Combine (18) and (19) together, we have,

$$\begin{cases} \sum_{k=1}^{m} \Big(\sum_{j=1}^{l} \big[\tilde{a}_{jk} \varphi_j(u_T + c) - a_{jk} \varphi_j(u_T) \big] \Big) \psi_k(v_T) = 0, \\ \sum_{k=1}^{m} \Big(\sum_{j=1}^{l} \big[\tilde{b}_{jk} \varphi_j(u_T + c) - b_{jk} \varphi_j(u_T) \big] \Big) \psi_k(v_T) = 0. \end{cases} \tag{20}$$

A sufficient condition for the existence of $\{\tilde{a}_{jk}\}_{j,k=1}^{l,m}$ and $\{\tilde{b}_{jk}\}_{j,k=1}^{l,m}$ is that the function space spanned by $\{\varphi_j(r)\}_{j=1}^{l}$ is exactly the space spanned by $\{\varphi_j(r+c)\}_{j=1}^{l}$. In this case, the coefficient terms for $\psi_k(v_T)$ can vanish in Ω. This condition holds true for polynomial basis $\{r^{j-1}\}_{j=1}^{l}$ and exponential basis $\{e^{c_j r}\}_{j=1}^{n}$. Therefore, the solutions given only v_T and function family constrains are not unique, further assumption should be applied.

B.2 Least Squares Initialization and Rank Analysis

Given N_p spatial points, the least squares problem for reaction term identification can be formulated as,

$$\boldsymbol{y} = X\boldsymbol{\beta} + \epsilon,$$

where,

$$X = \begin{bmatrix} \Phi_u(u_1, v_1) & 0 \\ 0 & \Phi_v(u_1, v_1) \\ \vdots & \vdots \\ \Phi_u(u_{N_p}, v_{N_p}) & 0 \\ 0 & \Phi_v(u_{N_p}, v_{N_p}) \end{bmatrix}, \quad \boldsymbol{\beta} = \begin{bmatrix} \boldsymbol{a} \\ \boldsymbol{b} \end{bmatrix}, \quad \boldsymbol{y} = \begin{bmatrix} -d_u \Delta u_1 \\ -d_v \Delta v_1 \\ \vdots \\ -d_u \Delta u_{N_p} \\ -d_v \Delta v_{N_p} \end{bmatrix}.$$

Here $\Phi_u(u, v) = [\phi_1(u, v), \cdots, \phi_n(u, v)]$ denotes basis evaluations. The solution $\hat{\boldsymbol{\beta}} = (X^\top X)^{-1} X^\top \boldsymbol{y}$ exists uniquely when,

$$\text{rank}(X) = 2n.$$

This condition requires spatial variations in v to sufficiently excite all basis functions. For degenerate patterns (e.g., uniform states), we employ the integral constraint to break translational symmetry.

B.3 Well-posedness Conditions

Let $\Omega \subset \mathbb{R}^2$ be a bounded domain with smooth boundary $\partial\Omega$. The general form of reaction-diffusion system is given as,

$$\begin{cases} \partial_t u_i - d_i \Delta u_i = f_i(u), & (x, t) \in \Omega \times (0, T), \\ \nabla u_i \cdot \nu = 0, & (x, t) \in \partial\Omega \times (0, T), \\ u_i(x, 0) = u_{i,0}(x), & x \in \Omega, \end{cases} \tag{21}$$

where $u = (u_1, u_2), d_i > 0$ are diffusion coefficients, ν is the unit outward normal vector on $\partial\Omega, u_{i,0}$ are bounded, non-negative initial data. Here, we study the global existence of classical solution to (21). Note that the nonlinearities satisfy the following conditions,

1. (Local Lipschitz continuity)$f_i : \mathbb{R}^2 \to \mathbb{R}$ is locally Lipschitz.

2. (Quasi-positivity) $f_1(0, u_2) \geqslant 0$, $f_2(u_1, 0) \geqslant 0$.
3. (Mass control) There exists a constant K such that
$$f_1(u) + f_2(u) \leqslant K(1 + u + v).$$
4. (Polynomial bounded) There exist $C > 0$ and $\mu > 0$ such that
$$f_1(u), f_2(u) \leqslant C\left(1 + |u|^{\mu}\right),$$
where $|u| = |u_1| + |u_2|$.

We first mathematically define the classical solution.

Definition B.1 (Classical Solution)**.** A vector-valued function $\mathbf{u} = (u_1, u_2)$ is called a classical solution to the system (21) on $\Omega \times (0, T)$ if we have for $i = 1$ and 2,

1. $u_i \in C^{2,1}(\Omega \times (0, T)) \cap C^0(\overline{\Omega} \times [0, T])$.
2. u_i satisfies each equation in (21) pointwise on $\Omega \times (0, T)$.

Let us first recall the classical local existence result under the above assumptions (Henry, 2006; Rothe, 2006)

Theorem B.2 (Local Existence)**.** *Assume that the nonlinearities f_i satisfy the assumptions 1, 2. For any bounded and non-negative initial data $u_{i,0} \in L^{\infty}(\Omega)$, $i = 1, 2$, there exists a time $T > 0$ such that the system (21) has a unique classical solution $\mathbf{u} = (u_1, u_2)$ on $\Omega \times (0, T)$. Moreover,*
$$\text{if } \limsup_{r \to T_{\max}} \|u_i(t)\|_{L^{\infty}(\Omega)} < \infty \text{ for all } i = 1, \ldots, m \text{ then } T_{\max} = +\infty. \tag{22}$$

Then we give the global existence results as follows.

Theorem B.3. *Assume that conditions 1–4 hold. Then for any bounded, nonnegative initial data, (21) has a unique nonnegative, global strong solution.*

The proofs could be found in (Morgan, 1989; Morgan & Tang, 2020).

C Turing Patterns and Reaction-Diffusion Systems

Reaction-diffusion systems describe the interaction between local reactions and spatial diffusion, leading to the emergence of complex spatiotemporal patterns. These models play a fundamental role in understanding self-organization across various scientific domains, including biology (Meinhardt & Gierer, 1974), chemistry (Zaikin & Zhabotinsky, 1970), and ecology (Rietkerk et al., 2021; Klausmeier, 1999). In this section, we review three classical reaction-diffusion models: the Gray-Scott (Gray & Scott, 1984), Brusselator (Prigogine & Lefever, 1968), and FitzHugh-Nagumo (FitzHugh, 1961) models, providing their mathematical formulations and explaining the characteristic patterns they generate.

C.1 Three Canonical Reaction-Diffusion Models

Gray-Scott Model

The Gray-Scott model describes an autocatalytic reaction system involving two interacting chemical species,
$$\frac{\partial u}{\partial t} = D_u \Delta u - uv^2 + F(1 - u),$$
$$\frac{\partial v}{\partial t} = D_v \Delta v + uv^2 - (F + k)v,$$
where u and v are the reactant concentrations, D_u and D_v are their respective diffusion coefficients, F is the feed rate, and k is the removal rate. The system exhibits a variety of spatiotemporal behaviors, including spot replication, stripe formation, and chaotic wave interactions.

BRUSSELATOR MODEL

The Brusselator model usually is used to describe chemical oscillations,

$$\frac{\partial u}{\partial t} = D_u \Delta u + a - (b+1)u + u^2 v,$$
$$\frac{\partial v}{\partial t} = D_v \Delta v + bu - u^2 v.$$

where a and b are control parameters governing the system's stability. When $b > 1 + a^2$, a Hopf bifurcation occurs, leading to sustained oscillations. The inclusion of diffusion introduces spatial inhomogeneities, resulting in Turing patterns.

FITZHUGH-NAGUMO MODEL

Derived as a simplification of the Hodgkin-Huxley equations for neuronal activity, the FitzHugh-Nagumo model describes excitable media,

$$\frac{\partial u}{\partial t} = D_u \Delta u + u(1-u)(u-a) - v,$$
$$\frac{\partial v}{\partial t} = D_v \Delta v + \epsilon(bu - v).$$

In this system, u represents the membrane potential, while v is the recovery variable. The parameters $a \in (0, 1)$ and $b > 0$ regulate excitability, and ϵ controls the time scale separation. The model supports traveling waves, pulse propagation, and wavefront interactions.

C.2 PATTERN FORMATION AND STABILITY ANALYSIS

Reaction-diffusion systems exhibit rich pattern formation behavior due to diffusion-driven instability. This section examines the conditions for instability and the mechanisms underlying pattern selection.

C.2.1 HOMOGENEOUS STEADY STATES AND STABILITY

A homogeneous steady state (u^*, v^*) satisfies the equilibrium conditions,

$$f(u^*, v^*) = 0, \quad g(u^*, v^*) = 0.$$

Linearize the system around (u^*, v^*), yielding the Jacobian matrix,

$$J_R = \begin{pmatrix} f_u & f_v \\ g_u & g_v \end{pmatrix}.$$

The stability of (u^*, v^*) in the absence of diffusion is determined by,

$$\text{tr}(J_R) = f_u + g_v < 0, \quad \det(J_R) = f_u g_v - f_v g_u > 0.$$

When diffusion is introduced, the dispersion relation for small perturbations takes the form,

$$\det(\lambda I - J_R + k^2 D) = 0,$$

where $D = \text{diag}(D_u, D_v)$ is the diffusion matrix.

C.2.2 TURING INSTABILITY AND PATTERN FORMATION

Turing instability occurs when a homogeneous steady state, stable in the absence of diffusion, becomes unstable due to spatial perturbations. The necessary conditions for this instability are,

$$\begin{cases} \text{tr}(J_R) < 0, \\ \det(J_R) > 0, \\ D_u g_v + D_v f_u > 2\sqrt{D_u D_v \det(J_R)}. \end{cases} \tag{23}$$

When these conditions hold, a band of wavenumbers k exists for which perturbations grow exponentially, leading to spatially periodic structures.

C.2.3 LINEAR STABILITY AND WAVELENGTH SELECTION

To determine the most unstable mode, we consider small perturbations of the form,

$$\begin{pmatrix} u \\ v \end{pmatrix} = \begin{pmatrix} u^* \\ v^* \end{pmatrix} + \epsilon \begin{pmatrix} \tilde{u} \\ \tilde{v} \end{pmatrix} e^{\lambda t + ikx}.$$

Solving for the growth rate λ yields

$$\det(\lambda I - k^2 D + J_R) = 0.$$

The wave number corresponding to the fastest-growing mode is given by,

$$k_c^2 = \frac{\det(J_R)}{D_u D_v}.$$

However, the system size L imposes constraints,

$$k_c \in \left[\frac{\pi}{L}, \frac{2\pi}{L}\right].$$

This determines the characteristic wavelength of the emergent pattern. Beyond the linear regime, nonlinear interactions influence the final pattern selection. Depending on system parameters, patterns may evolve into spots, labyrinthine structures, or traveling waves.

The onset of diffusion-driven instability can be analyzed by considering the perturbed system,

$$\frac{\partial}{\partial t} \begin{pmatrix} \hat{u} \\ \hat{v} \end{pmatrix} = \begin{pmatrix} D_u k^2 & 0 \\ 0 & D_v k^2 \end{pmatrix} \begin{pmatrix} \hat{u} \\ \hat{v} \end{pmatrix} + J_R \begin{pmatrix} \hat{u} \\ \hat{v} \end{pmatrix}.$$

The system is unstable if the real part of at least one eigenvalue becomes positive for some wavenumber k, leading to pattern formation.

D IMPLEMENTATION DETAILS

D.1 ALGORITHM

The following pseudocode(1) outlines our approach.

D.2 DISCRETIZATION

The numerical simulations were conducted on a uniform 75×75, 100×100, 150×150 spatial grid. We employed a second-order central difference scheme to approximate the Laplacian operator. For spatial coordinates (i, j), the discretized system takes the form

$$\frac{\partial u_{i,j}}{\partial t} = d_u \left(\frac{u_{i,j-1} + u_{i,j+1} + u_{i-1,j} + u_{i+1,j} - 4u_{i,j}}{(\Delta x)^2} \right) + f(u_{i,j}, v_{i,j}),$$
$$\frac{\partial v_{i,j}}{\partial t} = d_v \left(\frac{v_{i,j-1} + v_{i,j+1} + v_{i-1,j} + v_{i+1,j} - 4v_{i,j}}{(\Delta x)^2} \right) + g(u_{i,j}, v_{i,j}),$$

where we assume uniform spatial discretization with $\Delta x = \Delta y$. The domain boundaries are treated with no-flux Neumann boundary conditions.

D.3 INITIAL CONDITIONS AND TIME INTEGRATION

The simulation initializes states with spatially structured perturbations,

$$\begin{aligned} u_{i,j}(0) &= u^* + \eta^u_{i,j}, \\ v_{i,j}(0) &= v^* + \eta^v_{i,j}, \end{aligned} \tag{24}$$

where (x_i, y_j) denote grid coordinates. This deterministic initialization ensures reproducible pattern formation while breaking spatial symmetry.

For time integration, we apply explicit Euler scheme. Fixed time step $\Delta t = 0.2$ with CFL constraint

$$\Delta t \leq \frac{(\Delta x)^2}{2 \max(D_u, D_v)}. \tag{25}$$

Algorithm 1 Hierarchical Optimization for Pattern Dynamics

Input: Observed state v, diffusion coefficients d_u, d_v
Output: Estimated state $\hat{u}$, reaction functions $\hat{f}, \hat{g}$
Stage 1: Initial Coefficient Estimation
for each local window Ω_w **do**
  Solve $\{a^0_{w,i}, b^0_{w,i}\} \leftarrow \arg\min \mathcal{L}_{\text{local}}(\Omega_w)$ {window-wise least squares}
end for
Aggregate global coefficients: $a^0_i \leftarrow \mathbb{E}_w[a^0_{w,i}]$, $b^0_i \leftarrow \mathbb{E}_w[b^0_{w,i}]$
Stage 2: Joint Optimization
Initialize $\boldsymbol{\theta}, \gamma \leftarrow 0$, $\{a_i, b_i\} \leftarrow \{a^0_i, b^0_i\}$
Set η_0, β, p, $k \leftarrow 0$
repeat
  Compute state estimate: $\hat{u} \leftarrow u_{NN}([v, \Delta v]; \theta)$
  Calculate $\alpha \leftarrow \text{sigmoid}(\gamma)$ {Adaptive mixing}
  Evaluate PDE residuals $\mathcal{R}_u$, $\mathcal{R}_v$:
  $\hat{f} \leftarrow \alpha f_{\text{NN}}(\hat{u}, v; \theta^{(t)}_f) + (1-\alpha)\sum_i a^{(t)}_i \phi_i(\hat{u}, v)$
  $\hat{g} \leftarrow \alpha g_{\text{NN}}(\hat{u}, v; \theta^{(t)}_g) + (1-\alpha)\sum_i b^{(t)}_i \phi_i(\hat{u}, v)$
  Compute $\mathcal{L}_{\text{total}} \leftarrow \sum \lambda_i \mathcal{L}_i$
  Update $\theta^{(k+1)}_u, \theta^{(k+1)}_f, \theta^{(k+1)}_g, \boldsymbol{a}^{(k+1)}, \boldsymbol{b}^{(k+1)}, \gamma^{(k+1)}$ via Adam
  $k \leftarrow k + 1$
until $\|\Delta\mathcal{L}\| < \epsilon$ **OR** $\|\Delta\boldsymbol{\theta}\| < \delta$
Output: Thresholded coefficients $\tilde{a}_i \leftarrow a_i \cdot \mathbb{I}(|a_i| > \tau)$

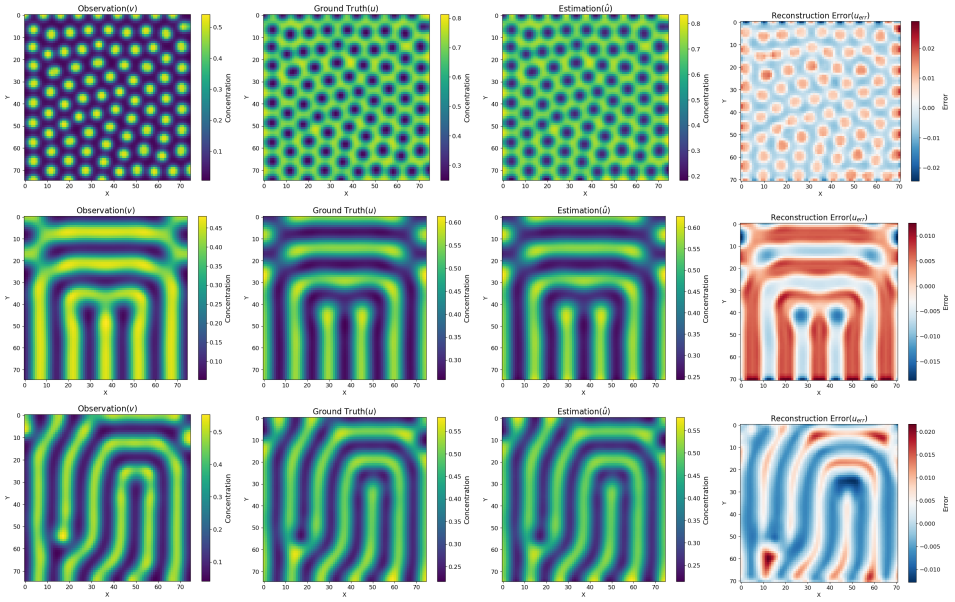

Figure 7: State reconstruction performance for Turing pattern models(75×75 grid). From top to bottom panel: dot, stripe, and maze patterns. From left to right panel: observed state, ground truth, estimated hidden state, reconstruction error.

E EXPERIMENT RESULTS

E.1 PATTERN RECONSTRUCTION

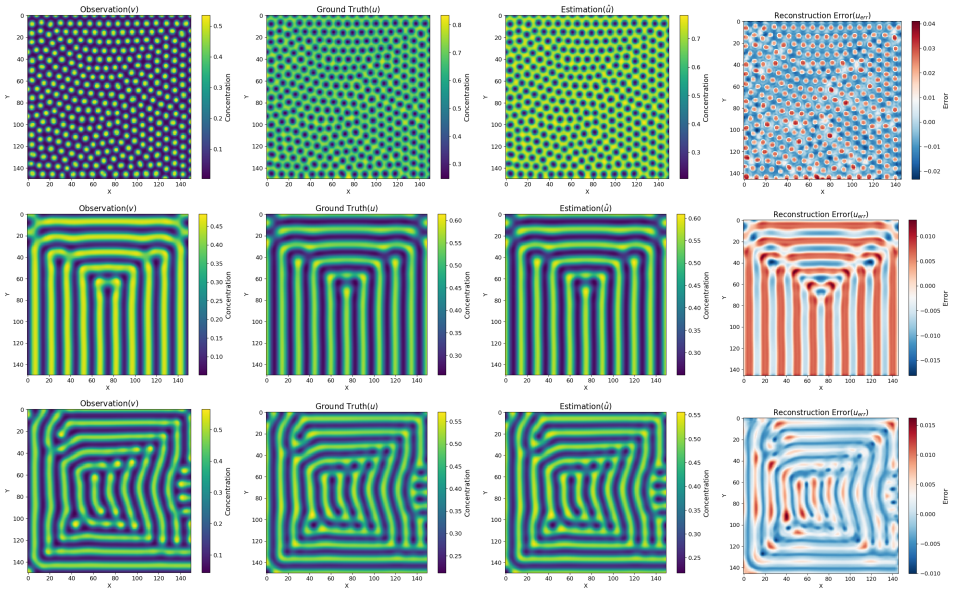

Figure 8: State reconstruction performance for Turing pattern models(150×150 grid). From top to bottom panel: dot, stripe, and maze patterns. From left to right panel: observed state, ground truth, estimated hidden state, reconstruction error.

E.2 ROBUSTNESS TO NOISE

We evaluate the robustness of reconstructing the reaction equations $f(u, v)$, $g(u, v)$, and hidden state $\mathbf{u}$ under varying noise conditions. The reconstruction error exhibits a controlled growth pattern as noise levels increase, with errors remaining bounded up to $\sigma = 0.2$. This behavior demonstrates the method's resilience to measurement uncertainties, particularly within the practical range of $\sigma \in [0.01, 0.15]$, where most real-world applications operate.

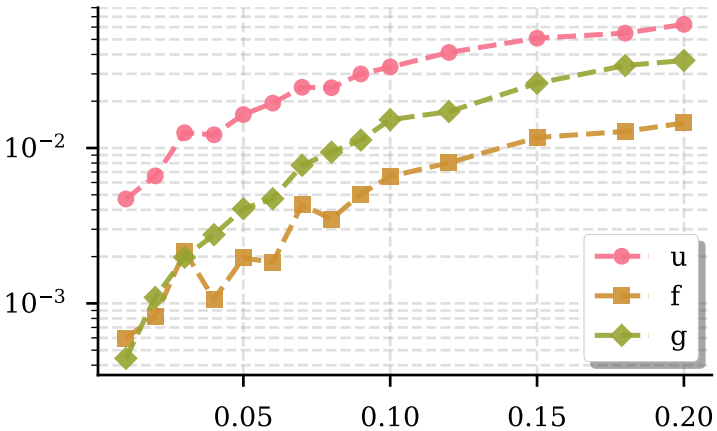

Figure 9: Sensitivity analysis of the reconstruction performance.

Figure 10 presents a detailed visualization of field reconstructions under four different noise scenarios ($\sigma = \{0.01, 0.05, 0.1, 0.15\}$). For each noise level, we show (a) the observed field, (b) the reconstructed field, and (c) the corresponding reconstruction error. At $\sigma = 0.01$, the reconstruction closely matches the observed field with minimal error patterns. We could observe that, as noise levels increase, the reconstruction quality gradually degrades, though the method maintains reasonable fidelity even at $\sigma = 0.15$.

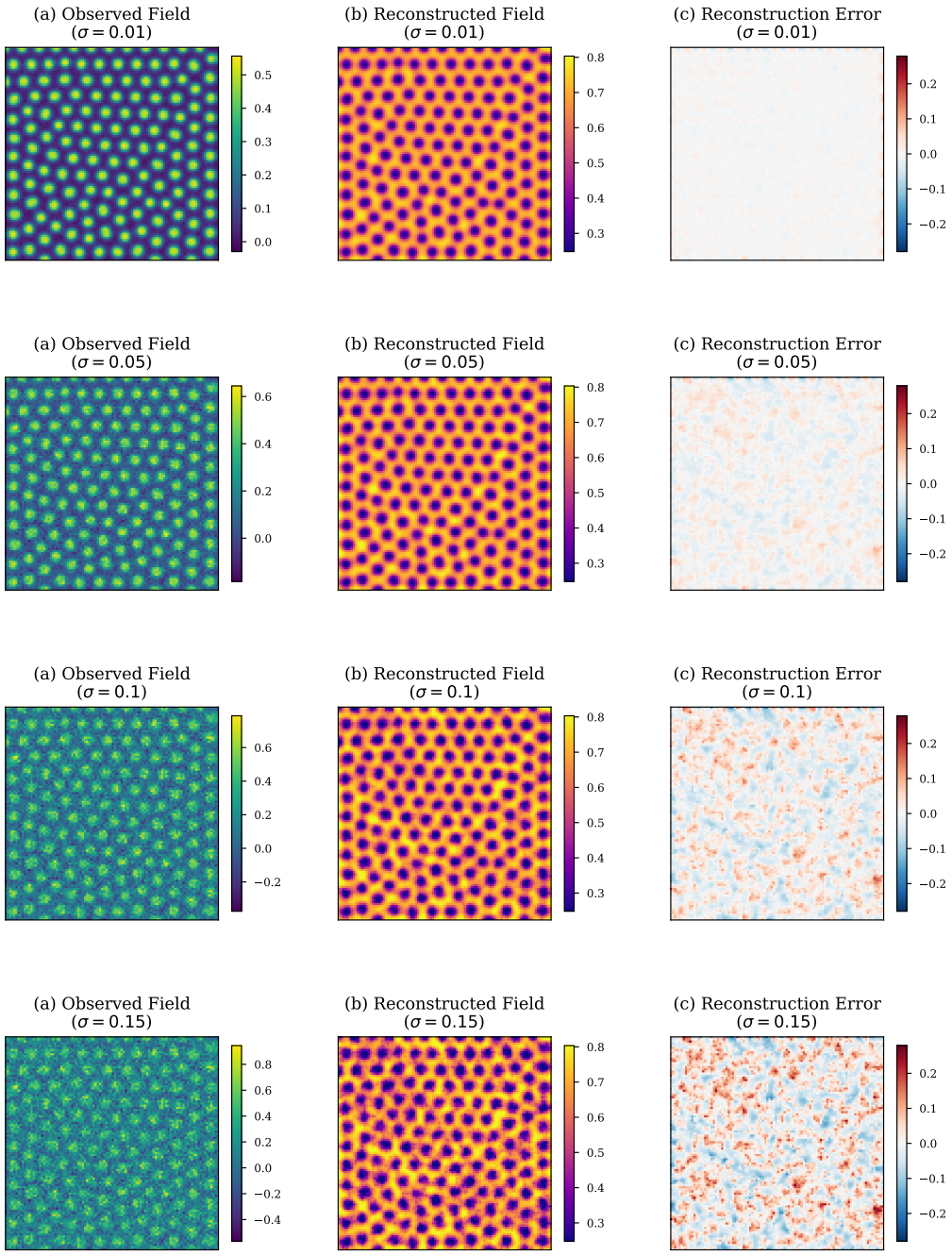

Figure 10: Comparison of field reconstructions under varying noise conditions.